Received: 31 January 2020 | Revised: 27 February 2020 | Accepted: 23 March 2020

DOI: 10.1002/aoc.5734

FULL PAPER

Applied Organometallic Chemistry WILEY

Single crystal X-ray of 1-[(1,2,4-triazole-4-yl)imino]diacetyl monoxime (L) as a novel triazole and the characterization and biological studies of its chelates of Co^{2+}, Pd^{2+}, and Fe^{3+}

Mohsen M. Mostafa | **Abdelmonem H. Elaskalany** | **Doaa E. El-Kkholy**

Chemistry Department, Faculty of Science, Mansoura University, Egypt

Correspondence
Mohsen M. Mostafa, Chemistry Department, Faculty of Science, Mansoura University, Egypt.
Email: mmostafa84@hotmail.com

A novel and efficient synthesis of 1-[(1,2,4-triazole-4-yl)imino]diacetyl monoxime (**L**) is described. The advantages of this method are that it is inexpensive, the starting reactants are readily available, and it has good yield and short reaction times. The hull of the product was suggested by elemental analyses, spectral and single crystal X-ray. Novel Co^{2+}, Pd^{2+}, and Fe^{3+} chelates derived from **L** were characterized by Fourier transform infrared spectroscopy, suggesting that **L** acts as bidentate via the two azomethine groups. Tetrahedral geometry for Fe^{3+} and Co^{2+} and square-planar geometry around the Pd^{2+} chelate were suggested depending on the spectral and magnetic data. The results of density functional theory were applied to illustrate the geometry of **L** towards the metal ions. Coats–Redfern and Horowitz–Metzger methods were applied to investigate the kinetic and thermodynamic parameters of the chelates. Cyclic voltammetry was carried out to study the stability of the Co^{2+} and Fe^{3+} chelates. **L** and its complexes were tested against three types of cancer cells, antibacterial and antifungal.

KEYWORDS

1-[(1,2,4-triazole-4-yl)imino]diacetyl monoxime (L), biological studies, single crystal X-ray, spectral studies

1 | INTRODUCTION

Derivatives of triazoles are applied as organic heterocyclic compounds that used as ligands containg several donor sites. 1,2,4-Triazole is a cyclic hydrazone that is synthesized with hydrogen atoms (or substitution) on either the hydrazide N atom or an amide N atom. In recent years 1,2,4-triazoles have gained significant attention as ligand systems due to the additional N-donor atoms that create mono-, bi-, or tridentate binding sites which improve the stability of complexes due to the chelation effect. Noncovalent interactions, such as dipole–dipole, hydrogen bonding lone pair (N)–π and π-stacking, can engage a large variety of 1,2,4-triazoles with biological targets.[1,2] The 1,2,4-triazole system and its derivatives have gained interest as ligands to transition metal ions since the coordination geometry of both pyrazoles and imidazoles acting as bridging ligands between two metal centers.[3] Various biological activities, such as antiasthamatic,[4,5] antiviral,[6] antifungal,[7] antimicrobial,[8] sandman,[9] pesticide,[10] mastectomy cancer preventive,[11,12] anticonvulsant, anticancer, anti-inflammatory,[13–22] Central nervous system depression,[23] antitumor,[24] and antihypertensive activities,[25,26] have been reported. *1,2,4*-Triazoles have plant growth regulating and anticogulant properties.[27] Three metal chelates with the general formulae $[Co\mathbf{L}Cl_2(EtOH)_{½}(H_2O)_{½}]$, $[Fe_2\mathbf{L}Cl_3(EtOH)_{½}]3Cl$, and $[Pd_2\mathbf{L}Cl_4(H_2O)_3]$ were synthesized and characterized by chemical, spectral (Fourier transform infrared [FT-IR], UV–visible [UV-Vis], ^{1}H NMR, ^{13}C NMR, Electron spin

resonance [EPR]), Thermal gravimetric analysis (TGA), and magnetic measurements. **L** and its chelates were tested against biological activity.

2 | EXPERIMENTAL

2.1 | Material and methods

All the compounds used in this investigation were of Analytical reagent (AR) quality and used as support. 2,3-Butanedione monoxime (BDH), hydrazine hydrate (Fisher Scientific), ethyl formate (Merck), anhydrous $FeCl_3$, $CoCl_2.6H_2O$, $PdCl_2$, DMSO, ether (BDH or Merck), ethanol (Fisher), HNO_3 (Aldrich), ethylenediaminetatraacetic acid disodium salt (EDTA), Eriochrome black T, and $AgNO_3$ were of AR quality and used as provided. Elemental analyses were determined in the Microanalytical Unit, Cairo University, Egypt. The percentages of iron, palladium, and chloride were determined using gravimetric methods while the cobalt content was determined by the volumetric method.[28] Spectral (IR, ^{1}H NMR, ^{13}C NMR, UV–Vis, EPR), magnetic, thermal, conductance, cyclic voltammetry, and single crystal measurements were carried out as reported earlier in our previous work.[29,30]

1-[(*1,2,4*-triazole-*4*yl)imino]diacetyl monoxime(**L**) (Figure 1) was prepared in two steps. First, 30 ml of hydrazine hydrate was added dropwise with shaking to 30 ml of ethyl formate in the presence of 30 ml of EtOH. The reaction mixture was refluxed with gentle heating and stirring for 8 hr. This solution was evaporated to one-third of its volume, then left to cool in an ice bath until the product formed. The resulting compound was crystallized several times using EtOH in the presence of charcoal. Finally, the solution was dried in a desiccator over $CaCl_2$. The melting point of this product was 65–68°C. In the second step 1.2 g of the first product was dissolved in 15 mLof EtOH and added to 2.02 g of 2,3-butanedione monoxime dissolved in 20 ml of EtOH in a few drops of glacial acetic acid. The reaction mixture was refluxed for 12 hr with gentle heating and continuous stirring, then the solution was evaporated to its half volume. Finally, the solution was left to cool at ambient temperature until the ligand precipitated out. Recrystallization was carried out several times by dissolving in the product in EtOH and filtering it over charcoal. The powdered product (m.p. 206–210°C) was dried in a vacuum desiccator over P_4O_{10}. White crystals with cubic shapes of the ligand were formed on leaving the filtrate for 2 weeks at room temperature (25°C). The product was colorless. Yield 70%, m.p. 208–210°C; ν_{max} (KBr): 3125 (s), 2980 (m), 2784 (w), 1678 (m), 1579 (m), 1509 (s), 1373 (s), 1210 (m), 1183 (m), 1129 (m), 1068 (s), 1027 (s), 983 (s), 860 (s), 776 (s), 677 (m), 647 (m), 621 (m), 497 (w),422 (w); δ_H (500 MHz, DMSO-d_6): 2.057 (3 H; s, CH_3, C=N–), 2.165 (3 H; s, CH_3, C=N–OH), 8.735 (H; s, CH), 12.418 (H; s, OH); δ_C 9.407 (CCH_3): 14.281 (CCH_3), 140.139 (CH=N), 153.95 (C=N–N), 171.196 (C=NOH). Anal. calcd for $C_6H_9N_5O$ 167.178 (%): C 43.11, H 5.43, N 41.90; found (%): C 43.52, H 5.85, N 41.91. The experimental value of the mass spectrum of **L** equals 168, which agrees with the molecular weight of the ligand (167.172).

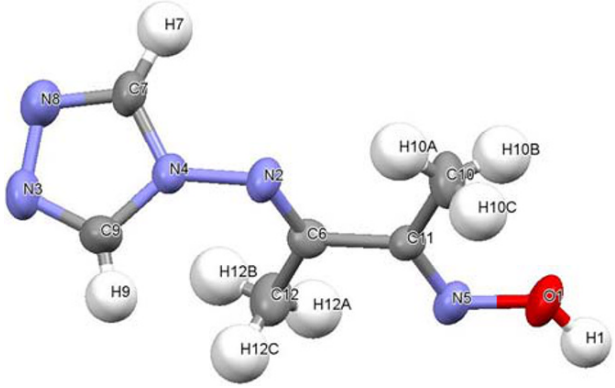

FIGURE 1 Structure of **L**

2.2 | Preparation of solid chelates

2.2.1 | Preparation of Fe^{3+} chelate

The ligand (1 mmol) was dissolved in10 ml of CH_3CN and 5 ml of EtOH and then added to a solution of $FeCl_3$ (1 mmol) dissolved in 10 ml of EtOH. The pH of the solution was 4 and it was refluxed with stirring on a hot plate for 12 hr. The mixture was evaporated on a water path almost to dryness until a brownish precipitate was obtained. The product was filtered off, washed several times with diethyl ether, and dried in a desiccator over P_4O_{10}. The general formula of the isolated Fe(III) chelate is $[Fe_2\mathbf{L}Cl_6(H_2O)_{½}(EtOH)_{½}]Cl_3$. Yield 50%, m.p. 220°C; brown powder,. Elemental analyses: anal. found for $C_7H_{13}Cl_6Fe_2N_5O_2$ (%): C 16.9, H 2.9, Cl 40.2, Fe 20.31; calcd (%): C 16.1, H 2.5, Fe 21.3, Cl 40.6. Λ_m (DMSO): 114 Ω^{-1} cm^2 mol^{-1} and μ_{eff}: 4.45 BM.

2.2.2 | Preparation of Co^{2+} chelate

$[Co\mathbf{L}Cl_2(H_2O)_{½}(EtOH)_{½}]$ was synthesized by mixing the ligand (0.167 g, 1 mmol) dissolved in a mixture of 10 ml of CH_3CN and 2 ml of EtOH to $CoCl_2.6H_2O$ (0.237 g, 1 mmol) de-iced in 10 ml of CH_3CN at pH 5–6). The reactants were kept under reflux with stirring on a hot plate for 5 hr and the color of the product changed from blue to bluish green. Finally, the resulting precipitate was filtered, washed with absolute EtOH followed by ether then

the product was kept in a vacuum desiccator over anhydrous P_4O_{10}. Yield 60%, m.p. 240°C. Elemental analyses: anal. found for $C_7H_{13}Cl_2Co\ N_5O_2$ (%): C 25.4, H 4.01, Co 18.8, Cl 21.9; calcd (%): C 25.6, H 4.0, Co 17.9, Cl 21.5. Λ_m: 30 $ohm^{-1}\ cm^2\ mol^{-1}$ and μ_{eff}: 4.3 BM.

2.2.3 | Synthesis of Pd^{2+} chelate

$[Pd_2\mathbf{L}Cl_4(H_2O)_3]$ was formed by mixing $PdCl_2$ (0.355 g, 2 mmol) dissolved in 25 ml of 3 moles of HCl. The reactants were refluxed for 5 min then the ligand (0.334 g, 2 mmol) dissolved in 10 ml of EtOH was added. The reaction mixture was acidic with pH 1. A deep yellow precipitate was formed at once then the reactant was refluxed with stirring on a hot plate for 5 hr. The resulting solid chelate was filtered off, washed with absolute EtOH and diethyl ether, and kept in a vacuum desiccator over anhydrous P_4O_{10}. Yield 60%, m.p. 240°C. Elemental analyses: anal. found for $C_6H_{15}Cl_4Pd_2N_5O_5$ (%): C 12.2, H 1.9, Pd 35.6, Cl 25.3; calcd (%): C 12.5, H 2.6, Pd 36.2, Cl 24.6. Λ_m: 12 $ohm^{-1}\ cm^2\ mol^{-1}$ and μ_{eff}: diamagnetic.

2.3 | Single-crystal X-ray crystallography

The crystallographic analysis of **L** was carried out using the same procedure as reported earlier.[29]

2.4 | Molecular modeling

2.5 | Computational details (molecular modeling)

The structures were performed by cluster calculations using the $DMOL^3$ program without any symmetry restriction in the Materials Studio Package, which is designed for the realization of large-scale density functional theory (DFT) calculations.[30,31]

2.6 | Biological activity

2.6.1 | Antibacterial and antifungal activity

The ligand and its compounds were tested against two antibacterials (Gram-positive, *Staphylococcus aurous*; Gram-negative, *Escherichia coli*) and two antifungals (*Candida albicans* and *Aspergillum flavus*) using the disc diffusion method.[32,33]

2.6.2 | Ant-hemolytic assay

The erythrocyte hemolysis procedure was applied as reported earlier.[34]

2.6.3 | Cytotoxic activity

The *in vitro* cytotoxicity of the ligand and some of its chelates was examined using 3-(4,5-dimethylthiazol-2-yl)-2,5-diphenyl tetrazolium bromide (MTT)-based assays. The colorimetric technique was used to determine cytotoxicity and to measure cell growth, as reported earlier.[29]

2.6.4 | Colorimetric assay for compounds that bind DNA

DNA methyl green (20 mg) was suspended in 100 ml of 0.05 M tris-HCl buffer (pH 7.5) containing 7.5 mM $MgSO_4$, then the mixture was stirred at 37°C for 24 hr. Test samples (10, 100, and 1000 mg) were dissolved in EtOH after that the solvent was separated under vacuum, and to each tube was added 200 µl of DNA/methyl green solution. Samples were incubated in the dark at ambient temperature. After 24 hr, the final absorbance of the samples was determined at 642.5–645 nm. The results were corrected for premier absorbance and normalized as the percentage of the untreated standard.

3 | RESULTS AND DISCUSSION

3.1 | IR spectra

The FT-IR spectrum of **L** in KBr (Supporting Information Figure S1) shows absorption bands at 3216(sh), 3125(s), 2980(m) and 2784(m) cm^{-1} which were attributed to OH, NH, CH, and CH_3, respectively. Three bands attributed to the azomethin groups (C=N) at 1678 cm^{-1} (C=NOH), 1658 cm^{-1} (C=N-N), and 1597 cm^{-1} (azomethin) triazole were relocated to lower wavelengths in the metal chelates, indicating the involvement of these groups in bonding. Two bands at 3216 and 3125 cm^{-1} were assigned to OH (free) and OH (hydrogen bonded). In the case of 2:1 (metal:ligand) chelates, the second metal ion (Pd^{2+} and Fe^{3+}) was coordinated via the triazole nitrogen (N–CH=N) as shown in Supporting Information Figures S2 and S3. The ligand coo167rdinates to the Co^{2+} ion through the two azomethin groups only (Supporting Information Figure S4). The appearance of broad weak bands in the 2000–2400 and 2500–2800 cm^{-1} regions

suggests the presence of interhydrogen bonding, as shown in Figure 2. The new band in the 437–459 cm^{-1} region was assigned to ν (M–N) vibration.[35] Peaks for the (M–O) bond in the Pd^{2+} and Fe^{3+} chelates were observed at 508 and 505 cm^{-1}, respectively. The ^1H NMR spectrum (Supporting Information Figure S5) exhibited two sharp singlet signals at 12.42 and 8.74 ppm due to the hydroxyl and CH groups, respectively, along with two singlet signals at 2.17 and 2.06 ppm indicating the presence of two CH_3 groups. The OH signal disappeared on adding D_2O, as shown in Supporting Information Figure S6. The ^{13}C NMR spectrum (Supporting Information Figure S7) shows five distinct singlet signals at 171.19, 153.95, 140.14, 14.28, and 9.41 ppm attributed to C=N-N, C=NOH, CH, H_3C–C=NOH, and H_3C–C=N–N, respectively. These results are in good agreement with the expected structure and the existence of hydrogen bonding (Figure 2). A possible reaction mechanism (Scheme 1) involving the formation of formic acid hydrazide by the reaction of ethyl formate with N_2H_4 in the presence of 1 mole of 2,3-butanedione monoxime and two drops of glacial acetic acid to produce [(3-(3H-1,2,4-triazole-4-(5*H*)-ylimino)butane-2-one-oxime (**L**) is proposed.

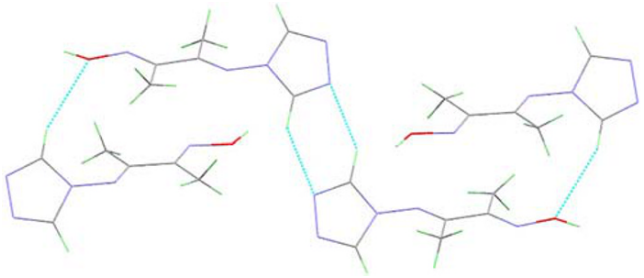

FIGURE 2 Hydrogen bonding in **L**

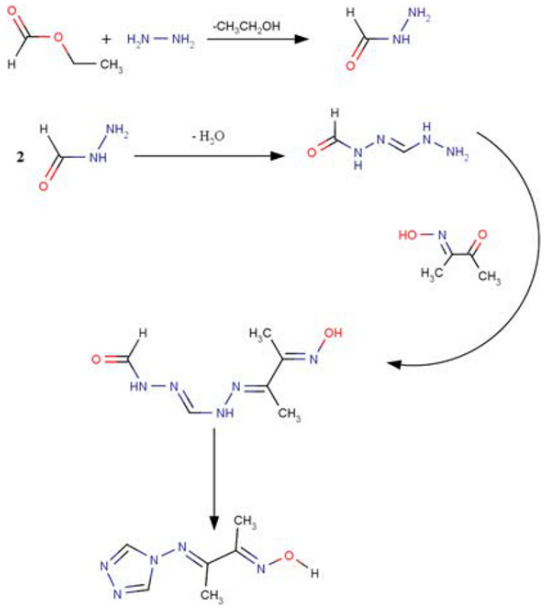

SCHEME 1 Reaction mechanism of 3-(3*H*-1,2,4-triazole-4-(5*H*)-ylimino)butan-2-one-oxime (**L**)

3.2 | X-ray structural analysis

Crystals elicited for single-crystalX-ray analysis were grown by slow evaporation of the reaction of ethyl formate and hydrazine hydrate in the presence of 1 mole of 2,3-butanedione monoxime and two drops of glacial acetic acid to produce 1-[(1,2,4-triazole-4-yl) imino]diacetyl monoxime (**L**). A view of the asymmetric crystal structure of the new ligand form is illustrated in Figure 3. The compound crystallizes in the orthorhombic space group **Pbca** with $Z = 8$ in the unit cell. The unit cell parameters of the title molecule have the following values: $a = 6.9624$ (4) Å, $b = 12.1261$ (8) Å, $c = 19.279$ (2) Å, and $\alpha = \gamma = \beta = 90$ (4), as shown in Table 1. The bond distances and angles are listed in Supporting Information Table S1. The crystal of the new ligand appeared in reptile form, the head consists of a triazole ring with two methyl groups as arms and an OH group as the tail; zigzag aliphatic chain with trans-methyl groups are perpendicular on flatten triazole ring which links to the chain through a central nitrogen atom. The molecules in the unit cell are interlinked through hydrogen bonds O–H ... N and C–H ... O is depicted in Figure 4 and the types of hydrogen bonding are shown in Table 2. The π ... π stacking between triazole rings by Cg1(N4-C7-N8-N3-C9) ... Cg2 (N8-N3-C9-N4-C7) with centroid–centroid distance 3.7 Å is recorded in Figure 5. The packing diagrams of the crystal along the *a*, *b*, and *c* planes are shown in Figure 6 having a chain structure.

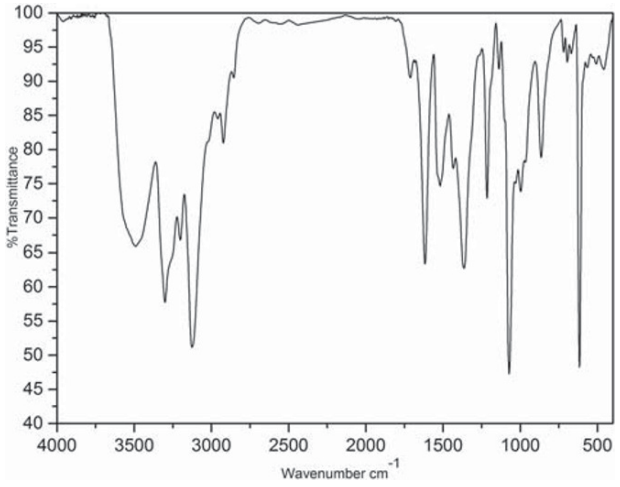

FIGURE 3 Perspective view of **L**

TABLE 1 Crystal data and structure refinement parameters of 3-(3*H*-1,2,4-triazole-4-(5*H*)-ylimino)butan-*2*-one oxime

Compound	L	
Empirical formula	$C_6H_9N_5O$	
Formula weight	167.178	
Temperature	298 K	
Wavelength	0.71073 Å	
Crystal system	Orthorhombic	
Space group	Pbca	
Unit cell dimensions	a = 6.9624 (4) Å	$\alpha = 90°$
	b = 12.1261 (8) Å	$\beta = 90°$
	c = 19.279 (2)Å	$\gamma = 90°$
Volume	1627.7 (2)Å^3	
Z	8	
Density (calculated)	1.460 Mg/m^3	
Theta range for data collection	30.17°	
Limiting indices	$h = 0 \rightarrow 9$, $k = 0 \rightarrow 16$, $l = 0 \rightarrow 27$	
R (int)	0.161	
Absorption correction	Multi-scanT_{min} = 0.876, T_{max} = 1.12	
Refinement method	Full-matrixleast-squares on F^2	
Data/restraints/parameters	339/0/133	
Final R indices [I > 3sigma(I)]	R (all) = 0.290, wR (ref) = 0.064	
R indices (all data)	R (gt) = 0.029, wR (all) = 0.130, wR (gt) = 0.064 S (ref) = 1.031, S (all) = 0.752, S (gt) = 1.031	
Calculated weights sigma	Δ/σ_{max} = 0.048, Δ/ρ_{max} = 0.96e A^3, Δ/ρ_{min} = −1.00e A^3	

3.3 | Spectral and magnetic measurements

The spectra of **L** and its Co^{2+}, Pd^{2+}, and Fe^{3+} chelates are depicted in Supporting Information Figures S8–S11. The electronic spectrum of the free ligand (Supporting Information Figure S8) shows bands at 45871, 41666, and 38759 cm^{-1}. The first two bands are attributed to $\pi \rightarrow \pi^*$ transitions while the last band refers to an $n \rightarrow \pi^*$ transition.[36] The Co^{2+} chelate (Supporting Information Figure S9) elucidates four bands, suggesting a tetrahedral structure around the Co^{2+} ion. The first band at 36496 cm^{-1} is due to an $n \rightarrow \pi^*$ transition, while the other three bands at 23041, 16233, and 14836 cm^{-1} are attributed to the $^4A_{2g} \rightarrow {}^4T_{1g}$(p) transitions.[37] The value of U_{eff} for the Co^{2+} chelate is 4.3 BM agrees with the suggested geometry for the Co(II) ion.[38,39] The visible spectrum of the Pd^{2+} complex (Supporting Information Figure S10) shows only one band at 26178 cm^{-1}, which can be attributed to the $^1A_{1g} \rightarrow {}^1B_{1g}$ transition in a square-planar geometry around the metal ion.[40] The diamagnetic nature of the Pd^{2+} chelate is taken as strong evidence of d^8 square-planar geometry. Finally, the electronic spectrum of the Fe^{3+} chelate in Nujol and DMSO (Supporting Information Figure S11a,b) shows two bands at 17605 and 18726 cm^{-1} (DMSO) and 24690 and 26109 cm^{-1} (Nujol). The first two bands are assigned to $^6A_1 \rightarrow {}^4T_1$ and $^6A_1 \rightarrow {}^4T_2$(G) transitions while the latter two bands are attributed to $^6A_1 \rightarrow {}^4E$, $^4A_1$ and $^6A_1 \rightarrow {}^4T_2$(D) transitions in a tetrahedral geometry. The value of the magnetic moment of the Fe(III) chelate (4.45 BM) suggests a tetrahedral geometry around the Fe^{3+} ion.[38,39]

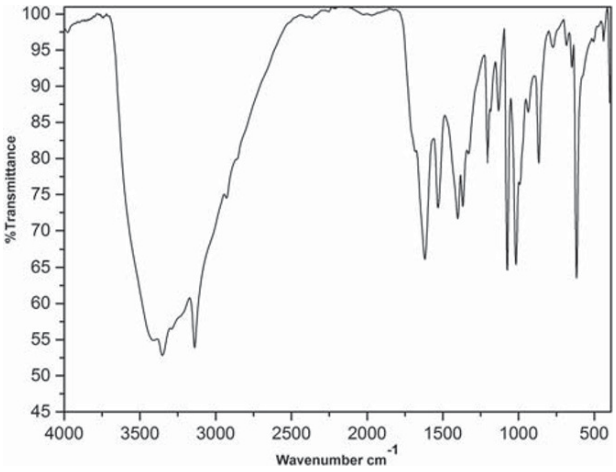

FIGURE 4 Hydrogen bond

3.4 | Thermal analysis

TGA plays important role in discussing the characteristics of the metal chelates. The curves are accomplished to make sure the suggested formulae and the structures of the complexes under investigation. TGA was performed from 20 to 1000°C and the results were used to evaluate and compute mass loss in addition to the results of the microanalyses. The decomposition steps for $[Pd_2\mathbf{L}Cl_4(H_2O)_3]$ are shown in Supporting Information Figure S12. The first step from 28 to 378°C occurs with the loss of three molecules of H_2O and three Cl ions (found 28.2%, calcd 27.9%). The second and third steps show losses in the region from 378 to 800°C corresponding to the fragments

TABLE 2 The unit cell inter-linked together through hydrogen bonds

D–H ... ...A	Symmetry	D–H (Å)	H ... ...A (Å)	D ... ...A (Å)	D–H .... A (°)
C12–H12Cii O1	x-1/2,y,1/2-z	0.920	2.95 (4)	3.557	108.95
C9–H9ii O1	x-1/2,y,1/2-z	0.942	2.67 (3)	3.657	66.85
C7– H7ii ... O1	x-1/2,y,1/2-z	1.091	2.93 (3)	3.252	81.78
C10–H10Aiii N2	1/2 + x,y,1/2-z	0.948	2.303 (4)	2.746	107.85
C10–H10Cii N2	x-1/2,y,1/2-z	0.941	2.93 (4)	2.746	140.03
O1– H1iv N3	x,1/2-y,z-1/2	0.960	1.781 (3)	2.737	173.66
C12–H12Cii N5	x-1/2,y,1/2-z	1.011	2.95 (3)	3.709	131.95
C7–H7v C7	1-x,-y,-z	1.091	2.71 (3)	3.337	116.35
C7–H7v N8	1-x,-y,-z	1.091	2.36 (4)	3.310	145.23
O1–H1iv N8	x,1/2-y,z-1/2	0.960	2.627 (4)	3.454	144.50
O1–H1iv C9	x, ½-y, z-½	0.960	2.743 (4)	3.552	159.28

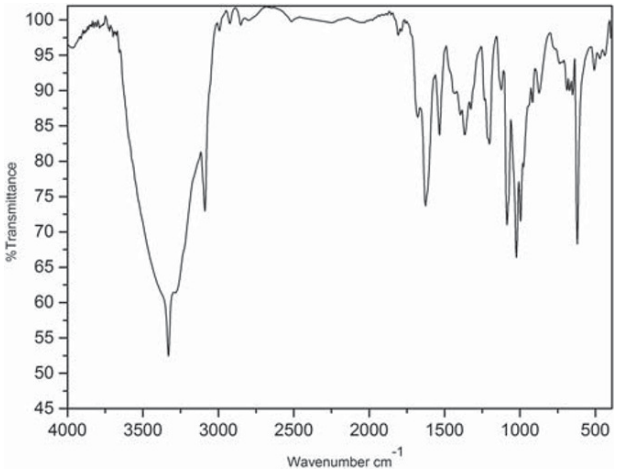

FIGURE 5 π–π stacking

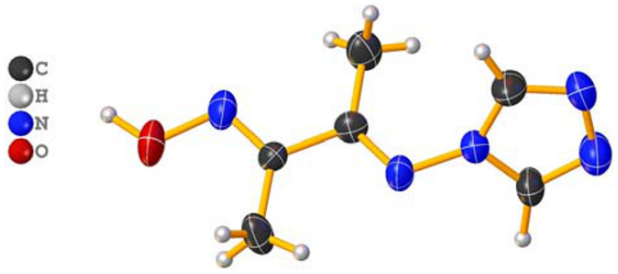

FIGURE 6 (**a**) Backing along the *a* axis, (**b**) backing along the *b* axis, and (**c**) backing along the *c* axis

H_9N_5Cl + 3C (found 26.66%, calcd 26.19%). The residue in the range 800–1000°C corresponds to $2PdC_3O$, in which the calculated loss of 45.9% matches the found loss of 45.2%. The chelates shown in Supporting Information Figures S13 and S14 show the TGA results of the other chelates and the thermal decomposition steps are tabulated in Table 3.

3.4.1 | TGA degradation steps and kinetic data for the Fe^{3+} and Pd^{2+} chelates

The kinetic data for the Fe^{3+} and Pd^{2+} chelates were estimated by Horowitz–Metzger[41] and Coats–Redfern[42] methods (Figures 7–9). Erying's equation[43] was used to calculate the thermodynamic parameters of activation and the results are recorded in Table 4 showing the following points:

i. The stages of decomposition illustrate the best fit for $n = 1$. Other values of n do not lead to best correlation.
ii. The free energy of the final residue is higher than that of the initial compound, illustrating from the positive value of ΔG^*, and the decomposition steps are nonspontaneous. The value of $T\Delta S^*$ exceeds than the value of ΔH^* since the ΔG^* values increase.[44,45]
iii. The affirmatory values of ΔH^* indicate that the behavior of all decomposition stages is endothermic.
iv. The ΔS^* values indicate that the decomposition steps are disordered structure for the energize fragments than of the undecomposed chelate and illustrating the slowness of the decomposition reaction.[43]

3.5 | Cyclic voltammetry

The redox properties of the Fe^{3+} and Co^{2+} chelates were investigated by cyclic voltammetry as shown in Figures 10 and 11, respectively. The measurements for the Fe^{3+} and Co^{2+} chelates (10^{-3} M) were officiated in nonaqueous DMF solution containing the supporting electrolyte 0.1 M of $[(n\text{-}Bu)_4N]PF_6$ within the potential range 1.6 to −0.2 V at scan rate 100 mV/s. The Fe^{3+}

TABLE 3 TGA decompositions steps for the metal chelates

Compound	Decomposition steps	Temperature range (°C)	Removed species	Weight loss (%)	
				Found	Calcd
$[Pd_2\mathbf{L}Cl_4(H_2O)_3]$	First	28–378	$3H_2O + 3Cl$	28.2	27.9
	Second	378–448	9H + Cl + 5 N	19.96	19.89
	Third	448–800	3C	6.7	6.3
	Residue	800–1000	2Pd + 3C + O	45.2	45.9
$[Fe_2\mathbf{L}Cl_6(H_2O)_{½}(EtOH)_{½}]$	First	30–121	$½H_2O + 4Cl$	28.79	28.8
	Second	121–466	2Cl + 3 N	21.99	21.57
	Third	466–800	5C + 2 N + 12H + 1½O	22.9	23.71
	Residue	800–1000	2Fe+2C	26.29	25.92
$[Co\mathbf{L}Cl_2(H_2O)_{½}(EtOH)_{½}]$	First	13–187	2C + 4H + N	12.59	12. 9
	Second	187–460	2Cl + 8H + 4 N + O	46.14	45.89
	Third	460–636	5C+ H	17.81	18.56
	Residue	636–1000	Co + O	23.46	22.78

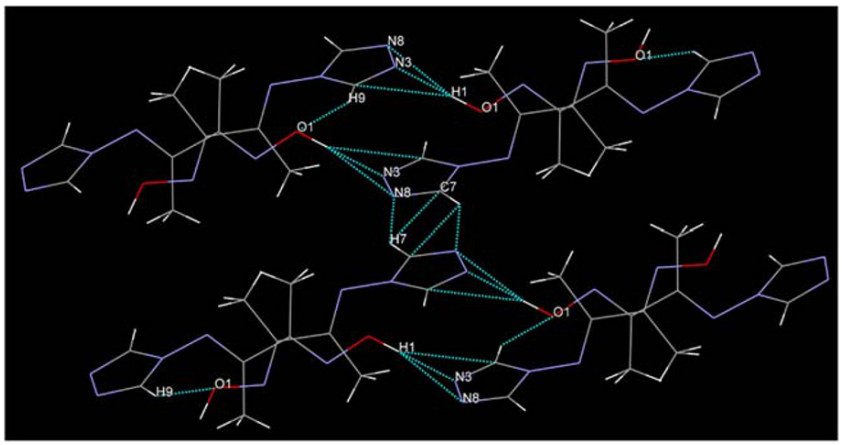

FIGURE 7 Coats–Redfern of (a), (a^-) and Horowitz–Metzger of (b), (b^-) first step of Pd^{2+} and Fe^{3+} chelates

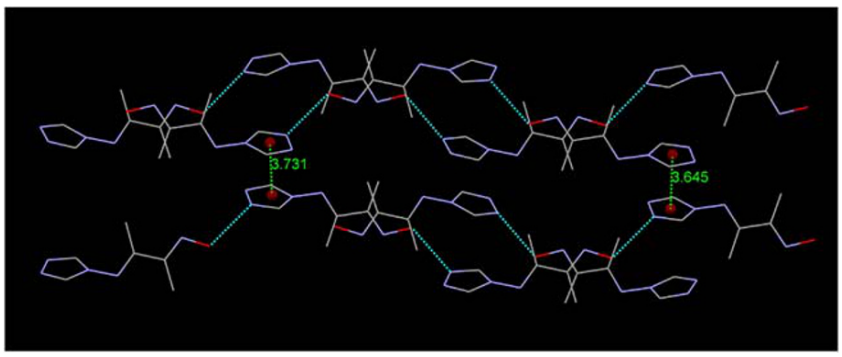

FIGURE 8 Coats–Redfern of (a), (b) and Horowitz–Metzger of (c), (d) second and third steps of Pd^{2+} chelate

chelate exhibited a quasi-reversible oxidation wave at positive potentials for one-electron transfer and $E_{1/2} = 0.125$ V and $\Delta E = 171$ mV, where $E_{pc} = +0.039$ V and $E_{pa} = +0.21$ V (Fe^{3+}/Fe^{2+}). The Co^{2+} chelate shows one irreversible oxidation peak of high oxidation current at $E_{pa} = +1.38$ V, which was assigned to the oxidation of Co^{2+} to higher oxidation states, for example Co^{4+}or Co^{5+}.

3.6 | Mass spectra

The experimental value of the mass spectrum of **L (**Figure 12**)** equals 168 which agrees with the molecular weight of the ligand (167.172). The peaks at m/z 68.16 and 14.23 with 100% and 14.43% abundance (calcd 68.06 and 41.03) correspond to the $[C_2H_2N_3]$ and $[CHN_2]$ fragments, respectively, and the dissociation

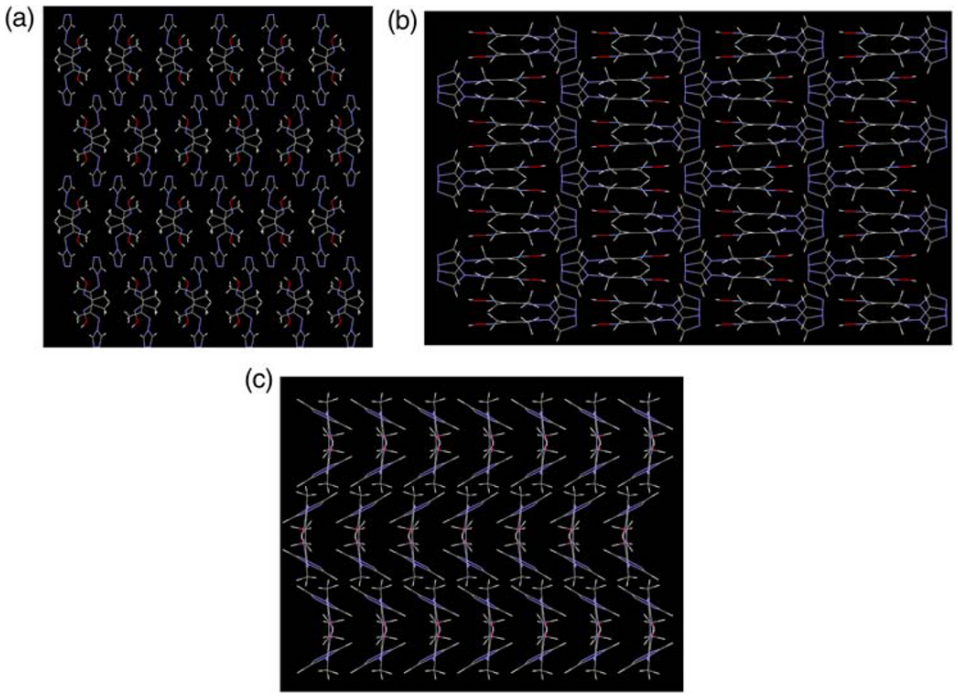

FIGURE 9 Coats–Redfern of (a), (b) and Horowitz–Metzger of (c), (d) second and third steps of Fe^{3+} chelate

TABLE 4 Kinetic parameters of Fe and Pd chelates evaluated by the Horowitz–Metzger(HM) and Coats-Redfern(CR) equations

Step	Mid temperature (K)	Method	E_a (kJ/mol)	$A(S^{-1})$	ΔH^* (kJ/mol)	ΔS^* (kJ/mol)	ΔG^* (kJ/mol)
Pd complex							
First	203	CR	101.40	1.02×10^{10}	98.53	−0.054	117.38
		HM	64.7	2.01×10^{6}	61.04	−0.146	126.27
Second	413	CR	199.89	1.66×10^{13}	195.26	0.003	193.59
		HM	173.4	1.13×10^{11}	167.65	−0.04	195.5
Third	624	CR	374.76	2.3×10^{24}	369.23	0.214	226.2
		HM	278.59	3.8×10^{7}	272.37	0.083	229.6
Fe complex							
First	76	CR	34.41	7.4×10^{3}	31.54	−0.191	97.63
		HM	40.29	6.1×10^{3}	37.34	0.173	99.06
Second	294	CR	35.92	35.01	31.29	0.220	154.02
		HM	46.39	6.07×10^{2}	42.47	−0.195	154
Third	633	CR	134.57	2.3×10^{6}	129.03	−0.129	215.23
		HM	147.8	1.8×10^{7}	141.1	−0.114	213.23

Arrhenius pre-exponential factor s^{-1}.

is shown in Scheme 2. The mass spectrum of [Co**L**-$Cl_2(H_2O)_{½}(EtOH)_{½}$] (Supporting Information Figure S12) shows a peak at m/z 330.6, which agrees with the estimated value (329.06), suggesting that the formula of the compound is emend. The fragmentation of the Co^{2+} chelate (1:1) is depicted in Supporting Information Scheme S1. The results of the elemental and thermal analyses were used to confirm the proposed formula. The spectrum shows the dissociation of Co(II) chelate (Figure S12).

The mass spectrum of [Fe_2**L**$Cl_3(H_2O)_{½}(EtOH)_{½}$]3Cl (Supporting Information Figure S16) shows a molecular ion peak at m/z 525.9, which agrees with the theoretical value (523.6). This shows that the suggested formula of this compound is agreed with the experimental data. Supporting Information Scheme S2 shows the fragments of the Fe^{3+}chelate (1:1). The data from the elemental and thermal analyses also are taken as evidence for that assumption. The mass spectrum indicates the dissociation of Fe chelate.

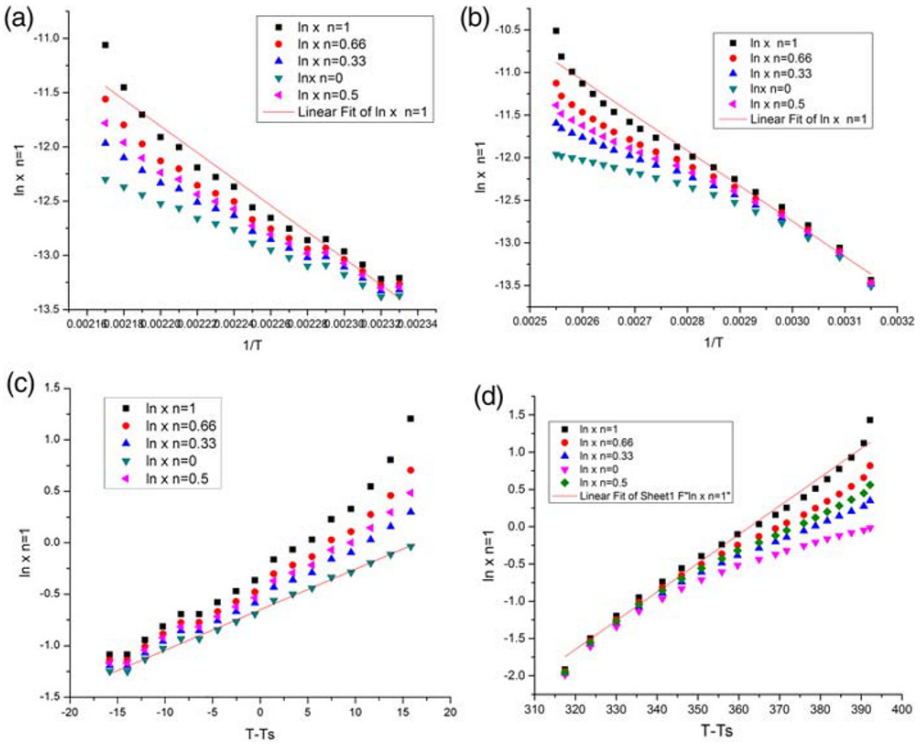

FIGURE 10 Cyclic voltammogram of Fe^{3+} chelate

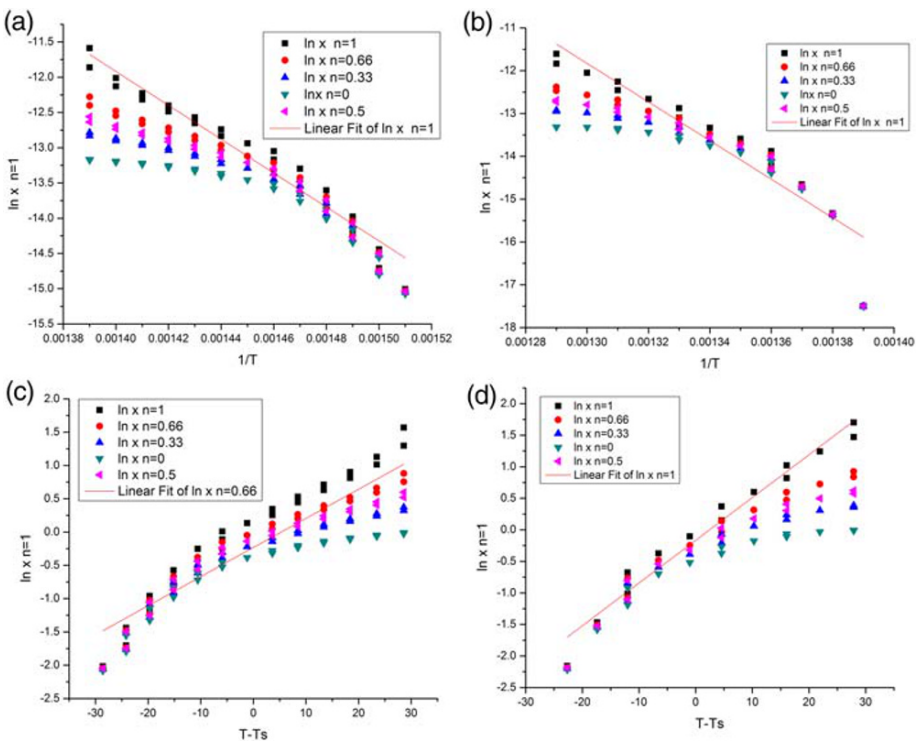

FIGURE 11 Cyclic voltammogram of Co^{2+} chelate

The mass spectrum of $[Pd_2\mathbf{L}Cl_4(H_2O)_3]$ has molecular ion peaks which is in agreement with its formula. The mass spectrum of $[Pd_2C_6H_9N_5OCl_4(H_2O)_3]$ shows fragmentation corresponding to the consecutive degradation of the complex. The first peak at m/z 576.62 with 13.69% abundance (Supporting Information Figure S17) represents the molecular ion peak (calcd 575.87). The peaks at m/z 450.0, 216.81, 69.05, and 55.11 with 10.8%, 19.49%, 30.66%, and 100% abundance (calcd 450.92, 215.52, 68.05, and 56.04) correspond to the $[Pd_2C_6H_9N_5OCl_2]$, $[PdC_4H_5N_4]^+$, $[C_2H_2N_3]^+$, and $[CH_2N_3]$ fragments, respectively. The successive degradation of the Pd^{2+} complex is shown in Supporting Information Scheme S3.

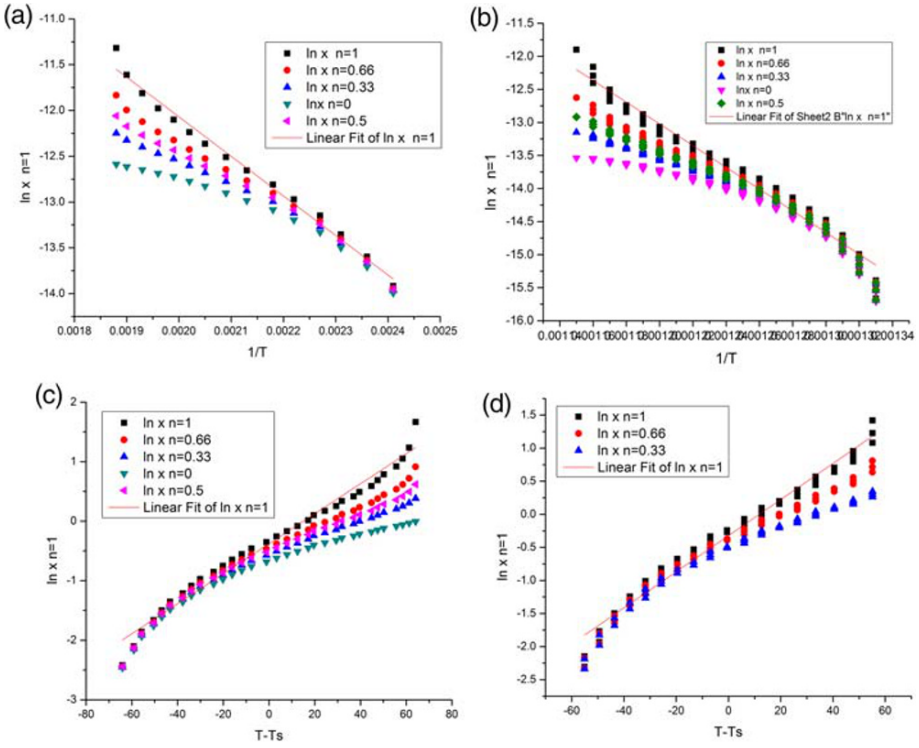

FIGURE 12 Mass spectrum of the free ligand

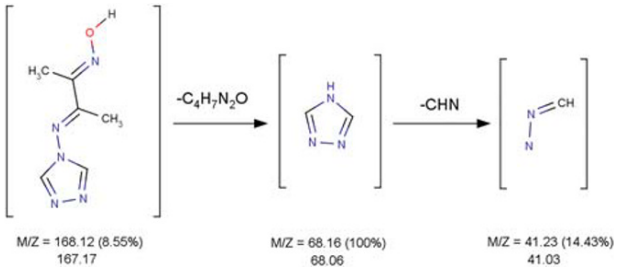

SCHEME 2 Fragmentation pattern of the ligand

3.7 | DFT calculation of molecular computation

The structures of **L** and its metal chelates showing the atom numbering are depicted in Supporting Information Figures S18–S21. The following statements can be made from examination of the bond angles and lengths:

i. The slightly longer bond distances of N(11)–C(30), N(12)–C(18), N(22)–C(24), and N(27)–C(29) in the chelates than in **L** is suggested from the formation of M–O and M–N bonds.
ii. Modification of the bond angles in **L** are decreased or increased on chelation to some extent upon coordination such as N(11)–N(34)–C(29), N(11)–N(34)–C(24), C(18)–C(30)–N(11), N(34)–C(29)–N(27), N(22)–N(27)–C(29), C(24)–N(22)–N(27), C(30)–C(18)–N(12), and C(1)–C(18)–N(12).
iii. The Co^{2+} and Fe^{3+} chelates have bond angles that support a tetrahedral geometry, while the Pd^{2+} chelate shows a square-planar geometry, where the bond lengths and bond angles of **L** are similar to these found from the X-ray diffraction analysis.
iv. The results in Table 5 indicate that the increase in molecular weight is followed by a decrease in energy in the gas phase.
v. The energies of the HOMO and LUMO are the essential parameters in quantum studies, in which the HOMO orbital acts as an electron donor and the LUMO orbital is an electron acceptor. These molecular orbitals are known as frontier molecular orbitals (FMOs) (Supporting Information Figures S18 and S21).

The results of the DFT explain the chemical reactivity and selectivity of the molecular systems. Both the energies of the FMOs (E_{HOMO} + E_{LUMO}) and the energy band gap (E_{HOMO} − E_{LUMO}) illustrate the end charge-transfer interaction within the molecule, electronegativity (χ), chemical potential (μ), global hardness (η), global softness (S), and global electrophilicity index (ω),[36,46,47] are listed in Table 5. The kinetic stability and chemical reactivity of the ligand and chelates depend on the energy difference (E_{HOMO} − E_{LUMO}), which is the former stability index that assists for the description. Soft compounds are those with small gap

TABLE 5 Calculated E_{HOMO}, E_{LUMO}, energy band gap (EH-EL), chemical potential (μ), electronegativity(X), global hardness (χ), global softness(S), and global electrophilicity index (ω) for **L** and its chelates

Compound	EH (eV)	EL (eV)	(EH-EL) (eV)	X (eV)	μ (eV)	χ (eV)	S (eV^{-1})	ω (eV)	σ (eV)
Lignad, $C_6H_9N_5O$	−5.845	−2.500	−3.345	4.17	−4.17	1.67	0.84	5.21	0.6
Co^{2+} chelate	−5.272	−3.922	−1.35	4.597	−4.59	0.68	0.34	15.49	1.47
Pd^{2+} chelate	−5.860	−4.021	−1.839	4.94	−4.94	0.92	0.46	13.26	1.09
Fe^{3+} chelate	−7.961	−7.581	−0.38	7.771	−7.77	0.19	0.09	158.88	5.26

that which is more reactive and more polarized than the hard compound due to its ease in donating electron to an acceptor.

3.8 | EPR studies

The powder EPR spectrum of the Fe^{3+} compound at ambient temperature (25°C) shows a spectrum suggesting that the Fe^{3+} ion has a tetrahedral structure. The breadth of the single line (H = 394 G) with g value 2.0032 supports a tetrahedral geometry in which the Fe^{3+} ion exists in a weakly tetrahedral structure.[48,49] The absence of the fine structure of Fe^{3+} (s = 5/2) is accepted with the tetrahedral structure.

3.9 | Biological studies

3.9.1 | Cytotoxic activity

The *in vitro* cytotoxicity of the ligand and some of its chelates was examined by MTT-based assays and the results are shown in Table 6.[38,50] Through colorimetric technique, MTT assay is considered a good method to determine cytotoxicity and measure cell growth. [MTT; *3-(4,5*-dimethylthiazol-*2*-yl)-*2,5*-diphenyl tetrazolium bromide] is yellow and on reduction changes to purple formazan via mitochondrial dehydrogenases of the cells. The purple formazan, which is insoluble, becomes soluble on addition of a suitable solvent to form the colored solution. Consequently, the absorbance at a specific wavelength of the colored solution was determined. In comparing the manipulated cells with the chelates and that obtained by unreacted control cells of the amount of purple formazan formed, as so we get the efficacy of the chelates in triggering death of cells concluded by the formation of a potion response curve. The data obtained show that the estimating of **L** has availed chemotherapy since it exhibits very strong activity towards mammary gland breast (MCF-7) and *Epitheliod* carcinoma cervix (Hela) with IC_{50} values of 7.91 and 6.83 μg/ml, respectively. The ligand also has strong activity against the prostate cell line PC-3 with an IC_{50} value of 12.13 μg/ml. On the other hand, the Pd^{2+} and Co^{2+} chelates have moderate IC_{50} values in PC-3 and MCF-7. The Fe^{3+} chelate has a weak IC_{50} value in the PC-3 and MCF-7 cell lines. In the Hela cell line $Fe^{3+}$and Co^{2+} chelates exhibit a moderate cytotoxicity effect, while the Pd^{2+}chelate has a weak IC_{50} value in the same cancer cell line. The extent of the activities of ligand and its chelates lies between very strong and moderate to weak, as shown in Figure 13.

TABLE 6 Cytotoxic activity of the ligand and metal chelates against human tumor cells

Compound	PC-3	MCF-7	Hela
DOX•	8.87	4.17	5.57
Ligand	12.13	7.91	6.83
Pd(II) complex	48.09	42.75	51.02
Fe(III) complex	59.54	73.13	38.91
Co(II) complex	45.80	31.26	29.28

Note. IC_{50} (μg/ml): 1–10, very strong; 11–20, strong; 21–50, moderate; 51–100, weak; above 100, noncytotoxic. DOX, doxorubicin.

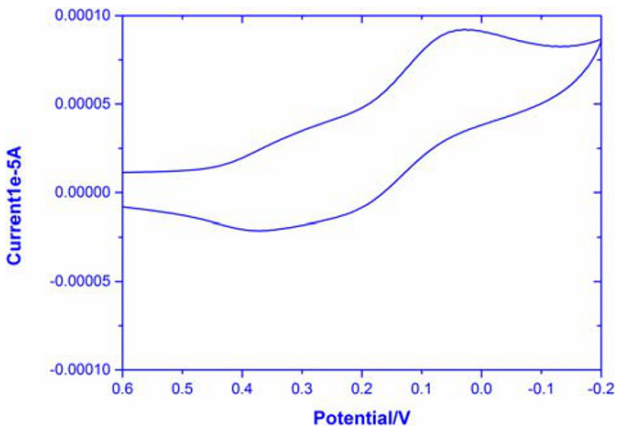

FIGURE 13 The scavenging capacities (IC_{50}) of the ligand and its metal chelates toward prostate cancer (PC-3), epithelioid carcinoma cervix cancer (Hela), and mammary gland breast cancer (MCF-7). Doxorubicin standard antitumor

3.9.2 | DNA/methyl green colorimetric assay of the DNA-binding compounds

Green methyl dye reacts with DNA to give a dyed DNA/methyl green compound in which the product of an addition reaction reversibly. This color does not change at neutral pH, whereas free methyl green obscured at this pH value. DNA-binding active compounds dislodge DNA from the methyl green complex**.** On alteration of DNA from methyl green by DNA inter-collators, so adding of water to the dye was allowed, that leading to development of the pale carbinol, then the absorbance declines colorimetric. The displacement was determined by a spectrophotometric assay as a decrease in the absorbance at 630 nm. The results were announced as inhibition concentration 50% value (IC_{50}) calculated by linear regression of data plotted on a semi-log scale and are shown in Table 7. In this assay doxorubicin was used as a control. The ligand displayed very strong inhibitory activity and powerfully intercalated DNA at a decreased IC_{50} value ranging from 29.18 ± 1.6 μM. The Co^{2+}, Fe^{3+}, and Pd^{2+} chelates have weak IC_{50} values of 56.94 ± 2.3, 61.40 ± 2.5, and 67.23 ± 2.4 μM, respectively.

3.9.3 | Antioxidant activities

The ligand (**L**) and its metal chelates were examined for their antioxidant activity by erythrocyte hemolysis. The screened antioxidant activity compared with vitamin C is depicted in Table 8 and Figure 14. The ligand exhibited high antioxidant activity. With respect to erythrocyte hemolysis, the activity of the tested chelates has the order Co(II) > Pd(II) > Fe(III) compared to vitamin C with respect to erythrocyte hemolysis.

TABLE 7 DNA binding activity of the ligand and its metal chelates

DNA active compound	DNA/methyl green (IC_{50}, μM)
DOX	31.27 ± 1.8
Ligand	29.18 ± 1.6
Co(II)	56.94 ± 2.3
Fe(III)	61.40 ± 2.5
Pd(II)	67.23 ± 2.4

Note. Values represent the concentration (mean ± SD, n = 3–5 separate determinations) required for a 50% decrease in the initial absorbance of the DNA/methyl green solution. DOX, doxorubicin.

TABLE 8 Antioxidant assay for the new compounds

No.	Compound	Erythrocyte hemolysis A/B × 100	
		Absorbance of samples (*A*)	% Hemolysis
Absorbance of H_2O (*B*)		0.875	–
Vitamin C		0.030	3.4%
1	Ligand	0.056	6.4%
2	Pd(II) chelate	0.134	15.3%
3	Fe(III) chelate	0.227	25.9%
4	Co(II) chelate	0.071	8.1%

3.9.4 | Antibacterial and antifungal activity

Ampicillin, an antibacterial agent and broad-field antibiotic, acted as a positive control for the antibacterial test, while DMSO was utilized as the negative control and solvent. The diameter of the inhibition zone of ampicillin towards *E. coli* is 25 mm and towards *S. aurous* is 21 mm. Table 9 shows the results of the antibacterial tests on the chelates towards Gram-negative*E. coli* and Gram-positive*S. aurous.* The Co(II) chelate has maximum antibacterial activity towards *E. coli* with an 18 mm inhibition zone diameter. The Pd(II) and Fe(III) chelates showed a sensible antibacterial activity towards *E. coli* with 12 and 11 mm inhibition zone diameters, respectively. The Co(II) chelate showed the strongest antibacterial activity of all the tested chelates towards *S. aurous* with a 19 mm inhibition zone diameter. The antibacterial effectiveness of the Pd(II) and Fe(III)

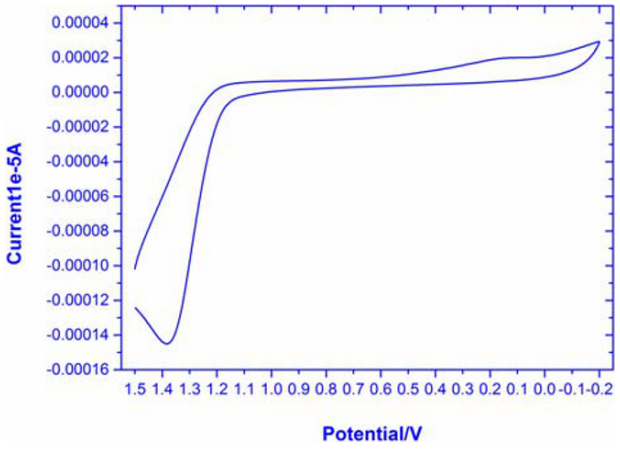

FIGURE 14 Antioxidant activities through erythrocyte hemolysis

TABLE 9 Antibacterial and antifungal inhibition zone diameter (mm/mg) of the ligand and its metal chelates

Sample		Inhibition zone diameter (mm/mg sample)							
		Bacteria				Fungi			
		E. coli (G^-)	% AI	*S. aureus* (G^+)	% AI	*A. flavus* (fungus)	% AI	*C. albicans* (fungus)	% AI
Standard	Ampicillin: antibacterial agent	25	100	21	100	–	–	–	–
	Amphotericin B: antifungal agent	–	–	–	–	17	100	21	100
Control: DMSO		0.0	0.0	0.0	0.0	0.0	0.0	0.0	0.0
Ligand		0.0	0.0	0.0	0.0	0.0	0.0	0.0	0.0
Co(II) chelate		18	72	19	90	0.0	0.0	13	62
Fe(III) chelate		11	44	14	66	0.0	0.0	0.0	0.0
Pd(II) chelate		12	48	13	61	0.0	0.0	10	47

Note. % AI, % activity index; G^-, Gram-negative; G^+, Gram-positive.

chelates against *S. aurous* was 13 and 14 mm, respectively. Amphotericin B (an antifungal agent) recorded antifungal activities towards the fungal strains *A. flavus* and *C. albicans* of 17 and 21 mm, respectively. The Co(II) and Pd(II) compounds showed moderate antifungal effectiveness towards *C. albicans* with 13 and 10 mm inhibition zone diameters, respectively. The Fe(III) chelate did not display any antifungal reactivity towards *C. albicans*. The Co(II), Fe(III), and Pd(II) compounds did not show any antifungal activity against *A. flavus.* It was perceived that the ligand has no effect against bacteria or fungi, as shown in Table 9. The antimicrobial activities of **L** and its chelates are shown in Figure 15. The efficiency and effectiveness propagation of compounds via cell membrane or interaction with microorganism cell wall give rise to a high antibacterial activity, which is known as lipophilic characteristics, that is, penetrating the lipid cell wall linked to the polarity of central metal ion and raised with formation of chelation ring which sharing the positive charge on metal ion with the N-donor atom of $\mathbf{L^1}$ causing π-electrondelocalization on the chelation ring also corroborate this (Figures 16–18).[51–53]

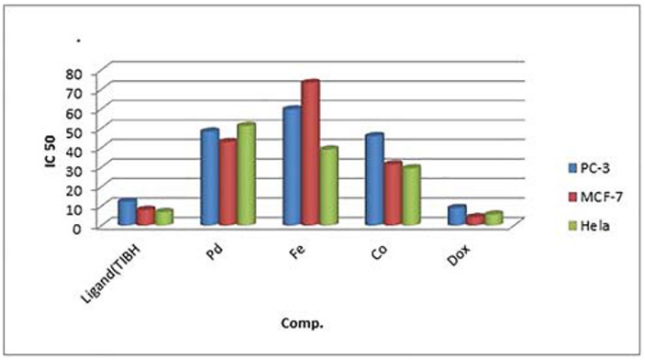

FIGURE 16 The scavenging capacities (IC_{50}) of the ligand and its metal chelates toward prostate cancer (PC-3), epithelioid carcinoma cervix cancer (Hela), and mammary gland breast cancer (MCF-7). Doxorubicin standard antitumor

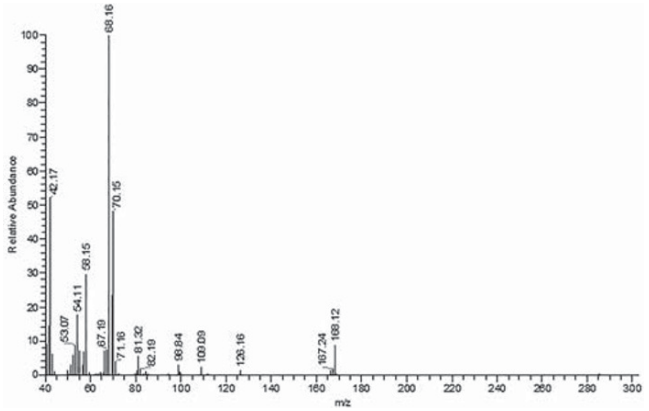

FIGURE 15 Antibacterial activity through erythrocyte hemolysis

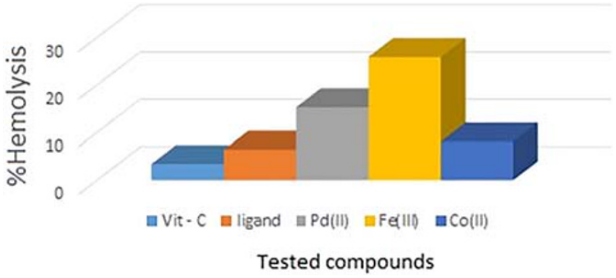

FIGURE 17 Antioxidant activities through erythrocyte hemolysis

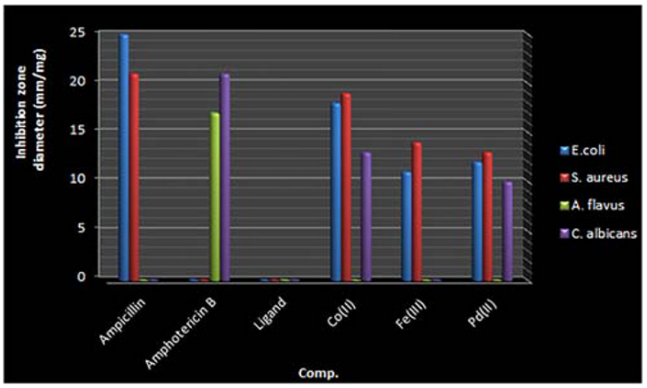

FIGURE 18 Antibacterial and antifungal activities of the ligand and its metal chelates

$$\%\text{activity index} = \frac{\text{zone of inhibition of test compound (diameter)}}{\text{zone of inhibition of standard (diameter)}} \times 100$$

4 | CONCLUSIONS

1-[(1,2,4-triazole-4-yl)imino]diacetyl monoxime (**L**) was synthesized for the first time by an indirect method and its structure was confirmed by single crystal X-ray. The ligand behaves in a bidentate manner via two azomethin groups towards metal ions. In 2:1 (metal: ligand) chelates, the second metal ion (Pd^{2+} and Fe^{3+}) is coordinated via the triazole nitrogen (N–CH=N). Spectral and magnetic results indicate a tetrahedral geometry around the Fe(III) and Co(II) ions while a square-planar structure was proposed for the Pd(II) chelate. The kinetic and thermodynamic parameters of the Fe^{3+} and Pd^{2+}chelates were investigated using the Coats–Redfern and Horowitz–Metzger methods. The redox properties of the Fe^{3+} and Co^{2+} chelates were studied by cyclic voltammetry, which provided information about the oxidation states of the Co^{2+} and Fe^{3+} chelates. Antibacterial and antifungal activity, antitumor activity, and cytotoxic activity showed that the ligand displays very strong inhibitory activity and powerfully intercalate DNA in comparison to its chelates.

X-ray data is registering CCDC 1590235 for *3*-(*3*H-*1,2,4*-triazole-*4*(*5*H)-ylimino)butan-*2*-one-oxime.

ORCID

Mohsen M. Mostafa https://orcid.org/0000-0003-3805-9107

REFERENCES

[1] G. Aromia, L. A. Barrosa, O. Rousseau, P. Gamez, *Coord. Chem. Rev.* **2011**, *255*, 485.
[2] C.-H. Zhou, Y. Wang, *Curr. Med. Chem.* **2012**, *19*, 239.
[3] J. G. Haasnoot, *Coord. Chem. Rev.* **2000**, *200*, 131.
[4] N. A. Al-Masoudi, Y. A. Al-Soud, I. A. Ali, *Nucleos. Nucleot. Nucl.* **2007**, *26*, 223.
[5] Y. Naito, F. Akahoshi, S. Takeda, T. Takada, M. Kajii, H. Nishimura, M. Sugiura, C. Fukaya, Y. Kagitani, *J. Med. Chem.* **1996**, *39*, 3019.
[6] E. De Clercq, *J. Clin. Virol.* **2004**, *30*, 115.
[7] X. Collin, A. Sauleau, J. Coulon, *Bioorg. Med. Chem. Lett.* **2003**, *13*, 2601.
[8] Z. Sui, J. Guan, D. J. Hlasta, M. J. Macielag, B. D. Foleno, R. M. Goldschmidt, M. J. Loeloff, G. C. Webb, J. F. Barrett, *Bioorg. Med. Chem. Lett.* **1998**, *8*, 1929.
[9] J. B. Hester, A. D. Rudzik, B. V. Kamdar, *J. Med. Chem.* **1971**, *14*, 1078.
[10] G. Tanaka, *Chem. Abstr.* **1975**, *82*, 156320h.
[11] P. A. Lambert, K. D. Somers, E. C. Kohn, R. R. Perry, *Surgery* **1997**, *122*, 372.
[12] H. T. Akçay, R. Bayrak, *Spectrochim. Acta a* **2014**, *122*, 142.
[13] M. Clemons, R. E. Coleman, S. Verma, *Cancer Treat. Rev.* **2004**, *30*, 325.
[14] O. Bekircan, H. Bektas, *Molecules* **2006**, *11*, 469.
[15] J. M. Kane, B. M. Baron, M. W. Dudley, S. M. Sorenson, M. A. Staeger, F. B. Miller, *J. Med. Chem.* **1990**, *33*, 2772.
[16] I. Küçükgüzel, S. G. Küçükgüzel, S. Rollas, G. Ötük-Sanis, O. Özdemir, I. Bayrak, T. Altug, J. P. Stables, *IL Farmaco* **2004**, *59*, 893.
[17] B. E. Gilbert, V. Knight, *Antimicrob. Agents Chemother.* **1986**, *30*, 201.
[18] B. S. Holla, B. Veerendra, M. K. Shivananda, B. Poojary, *Eur. J. Med. Chem.* **2003**, *38*, 759.
[19] G. Turan-Zitouni, M. F. Sivaci, S. Kiliç, K. Erol, *Eur. J. Med. Chem.* **2001**, *36*, 685.
[20] O. Bekircan, M. Kucuk, B. Kahveci, S. Kolayli, *Arch. Pharm.* **2005**, *338*, 365.
[21] P. C. Wade, B. R. Vogt, T. P. Kissick, L. M. Simpkins, D. M. Palmer, R. C. Millonig, *J. Med. Chem.* **1982**, *25*, 331.
[22] A. K. Gruta, K. P. Bhargava, *Pharmazie* **1978**, *33*, 430.
[23] B. Modzelewska, J. Kalabun, *Pharmazie* **1999**, *54*, 503.
[24] W. E. Meyer, A. S. Tomcufcik, P. S. Chan, M. Haug, *J. Med. Chem.* **1989**, *32*, 593.
[25] A. A. Siddiqui, R. Mishra, M. Shaharyar, A. Husain, M. Rashid, P. Pal, *Bioorg. Med. Chem. Lett.* **2011**, *21*, 1023.
[26] Y. A. Al-Soud, M. N. Al-Dweri, N. A. Al-Masoudi, *IL Farmaco* **2004**, *59*, 775.
[27] R. Elliott, R. L. Sunley, D. A. Griffin, *UK. Pat. Appl. GB.* **1986**, *2*, 175301.
[28] A. I. Vogel, *Text books of quantitative chemical analysis*, 5th ed., Longmans, London **1991**.
[29] (a) W. H. Al-Assy, M. M. Mostafa, *Spectrochim. Acta Part A* **2014**, *120*, 568. (b) W. H. Al-Assy, M. M. A. Mohamed, D. Z. Husien, M. M. Mostafa, *Spectrochim. Acta Part A* **2019**, *33*, 1. (c) E. A. Hassan, N. Nawar, M. M. Mostafa, *Spectrochim. Acta Part A* **2019**, *33*, 1.

[30] A. Altomare, G. Cascarano, C. Giacovazzo, A. Guagliardi, M. C. Burla, G. Polidori, M. Camalli, *J. Appl. Crystallogr.* **1994**, *27*, 435.
[31] (a) B. Delley, *J. Chem. Phys.* **1990**, *92*, 508. (b) B. Delley, *J. Chem. Quant. Chem.* **1998**, *69*, 423. (c) B. Delley, *J. Chem. Phys.* **2000**, *113*, 7756. (d) X. Wu, A. K. Ray, *Phys. Rev.* **2002**, *65*, 85403. (e) A. Kessi, B. Delley, *Int J. Quant. Chem.* **1998**, *68*, 135.
[32] Y. Morimoto, K. Tanaka, Y. Iwakiri, S. Tokuhiro, S. Fukushima, Y. Takeuchi, *Biol. Pharm. Bull.* **1995**, *18*, 1417.
[33] T. Mosmam, *J. Immunol. Methods* **1983**, *65*, 55.
[34] H. J. Mauceri, N. N. Hanna, M. A. Beckett, D. H. Gorski, M. J. Staba, K. A. Stellato, K. Bigelow, R. Heimann, S. Gately, M. Dhanabal, G. A. Soff, V. P. Sukhatme, D. W. Kufe, R. R. Weichselbaum, *Nature* **1998**, *394*, 287.
[35] A. P. Wilson, in *Cytotoxicity and viability assays in animal cell culture: A practical approach*, 3rded. (Ed: J. R. W. Masters), Oxford University Press, New York **2000**.
[36] A. U. Rahman, M. I. Choudhary, W. J. Thomsen, *Bioassay techniques for drug development*, CRC Press, Taylor and Francis Group, Amsterdam **2001**.
[37] J. R. Ferraro, *Low frequency vibration of inorganic and coordination compounds*, Plenum Press, New York **1971**.
[38] R. Parthasarathi, J. Padmanabhan, U. Sarkar, B. Maiti, V. Subramanian, P. K. Chattaraj, *J. Mol. Struct.* **2003**, *2*, 798.
[39] A. B. P. Lever, *Inorganic electronic spectroscopy*, Elsevier, Amsterdam **1968**.
[40] N. S. Al Radadi, S. M. Al-Ashqar, M. M. Mostafa, *Synth. React. Inorg. Met-Org Nano Met. Chem.* **2011**, *41*, 203.
[41] B. N. Figgis, J. Lewis, J. Wilkins, *Modern coordination chemistry*, Interscince, New York **1960**.
[42] D. Niholls, *Complexes and first row transition elements*, Macmillan, UK **1986**.
[43] H. H. Horowitz, G. Metzeger, *Anal. Chem.* **1963**, *35*, 1464.
[44] A. Coats, J. Redfern, *Nature* **1964**, *201*, 68.
[45] A. A. Frost, R. G. Pearson, *Kinetics and mechaanisms*, Wiley, New York **1961**.
[46] P. B. Maravalli, T. R. Goudar, *Thermochim. Acta* **1999**, *235*, 35.
[47] K. K. M. Yussuf, R. Sreekala, *Reaction Kinetics Mechanism and Catalysis* **1992**, *48*, 575.
[48] R. G. Pearson, *J. Org. Chem.* **1989**, *54*, 1423.
[49] J. Padmanabhan, R. Parthasarathi, V. Subramanian, P. Chattaraj, *J. Phys. Chem.* **2007**, *111*, 1358.
[50] (a) T. Mosmann, *J. Immunol. Methods* **1983**, *65*, 55. (b) F. Denizot, R. Lang, *J. Immunol. Methods* **1986**, *22*, 271. (c) M. I. Thabrew, R. D. Hughes, I. G. McFarlane, *J. Pharm. Pharmacol.* **1997**, *49*, 1132.
[51] Z. H. Chohan, *Synth. React. Inorg. Met. Org. Chem.* **2004**, *34*, 833.
[52] Z. H. Chohan, C. T. Supuran, A. Scozzafava, *J. Enzyme Inhib. Med. Chem.* **2004**, *19*, 79.
[53] aZ. H. Chohan, M. Arif, M. A. Akhtar, C. T. Supuran, *Bioinorg. Chem. Appl.* **2006**, *2006*, 1. bJ. M. Kane, B. M. Baron, M. W. Dudley, S. M. Sorensen, M. A. Staeger, F. P. Miller, *J. Med. Chem.* **1990**, *33*, 2772. cA. G. Altomare, G. Cascarano, C. Giacovazzo, A. Guagliardi, M. C. Burla, G. T. Polidori, M. Camalli, *J. Appl. Crystallogr.* **1994**, *27*, 435.

SUPPORTING INFORMATION

Additional supporting information may be found online in the Supporting Information section at the end of this article.

How to cite this article: Mostafa MM, Elaskalany AH, El-Kkholy DE. Single crystal X-ray of 1-[(1,2,4-triazole-4-yl)imino]diacetyl monoxime (L) as a novel triazole and the characterization and biological studies of its chelates of Co^{2+}, Pd^{2+}, and Fe^{3+}. *Appl Organomet Chem*. 2020;e5734. https://doi.org/10.1002/aoc.5734